








# Oxide Membranes from Bulk Micro-Machining of $\text{SrTiO}_3$ substrates

Nicola Manca <sup>1,2,\*</sup> Alejandro E. Plaza <sup>1,2</sup> Leonélio Cichetto Jr <sup>1</sup>  
Warner J. Venstra <sup>3</sup> Cristina Bernini <sup>1,2</sup> Daniele Marré <sup>4,1</sup> and Luca Pellegrino <sup>1,2</sup>

<sup>1</sup>CNR-SPIN, C.so F.M. Perrone, 24, 16152 Genova, Italy

<sup>2</sup>RAISE Ecosystem, Genova, Italy

<sup>3</sup>Quantified Air BV, Langegracht 70, 2312NV Leiden, The Netherlands

<sup>4</sup>Dipartimento di Fisica, Università degli Studi di Genova, 16146 Genova, Italy

Suspended micro-structures based on complex oxides relies on surface micro-machining processes such as those based on sacrificial layers. These processes prevent to physically access the microstructures from both sides, as substantial part of the substrate is not removed. In this work, we develop a bulk micromachining protocol of a commonly used substrate employed in oxide thin film deposition. We realize suspended oxide thin film devices by fabricating pass-through holes across  $\text{SrTiO}_3(100)$  or  $\text{SrTiO}_3(110)$  substrates. Careful calibration of anisotropic etching rates allows controlling the final geometry of the aperture in the substrate in a predictable way. As demonstrators of possible device geometries, we present clamped membranes and trampolines of  $(\text{La,Sr})\text{MnO}_3$ , a conductive magnetic oxide, and a suspended trampoline resonator carved from the  $\text{SrTiO}_3$  substrate itself. Reported protocols can be readily extended to a broad variety of other complex oxides so to extend the application of membranes technology beyond those of commercially-available silicon compounds.

## I. INTRODUCTION

The realization of suspended or freestanding structures made of oxide thin films has recently triggered new experiments with complex oxides. The release processes from the growth substrate took inspiration from the experimental protocols developed for Van der Waals materials and silicon micro-electro-mechanical systems. Proposed approaches include the release of oxide membranes from their growth substrate by using various sacrificial layers [1–5], even water-soluble [6], the fabrication of superconducting oxide interfaces by spalling [7, 8], the integration of complex oxides with silicon suspended structures [9–15], or the fabrication of suspended oxide structures by etching their growth substrate [16, 17]. These results enabled new kind of experiments, taking advantage from the lower thermal dissipation of suspended thin films [18, 19], the possibility to apply large strain [20, 21], or from the measurement of the mechanical modes of oxide-based resonators [22, 23]. Applications where suspended oxides are particularly promising include pressure and gas sensors [24, 25], mechanical resonators [26, 27], bolometers [28, 29], nano-actuators [30, 31], piezoelectric devices [32, 33], or photo-strictive systems [34].

However, all these examples are based on the paradigm of surface micro-machining, while actual bulk micro-machining, i.e. the possibility to shape the growth substrate considering its whole thickness, is still missing. This is an enabling technology developed for silicon substrates processing resulting in a variety of applications, such as the integration of proof masses in accelerometers, gyroscopes, or seismic sensors, the fabrication of large membrane, the 3D integration by wafer

bonding, and physical access from backside, e.g. to enable optical readout [35, 36].

Here, we present a fabrication protocol to realize suspended devices from oxides thin films with pass-through holes on their back-side. This process is based on the wet chemical etching of the growth substrate across its full thickness. We discuss the general aspects of bulk micro-machining for  $\text{SrTiO}_3(001)$  and  $(110)$  cases, devoting a particular care in analyzing their anisotropic etching rates. We then show three examples of suspended oxide devices that can be realized with this protocol: trampoline resonators with controlled backside aperture width, sealed membranes, and trampoline resonators carved from the  $\text{SrTiO}_3$  substrate itself.

## II. RESULTS AND DISCUSSION

The fabrication protocol presented in this work relies on the selective wet chemical etching of  $\text{SrTiO}_3$  (STO). Its key element is the use of double-polished STO substrates having epitaxial thin films grown on both sides. These films are employed as hard masks during the substrate wet etching or even as device layers to realize fully suspended oxide structures. The use of oxide films as hard mask is due to their perfect adhesion provided by epitaxial growth. This is not the case for polymers deposited by spin coating or metal layers grown by thermal evaporation, which typically detach during the long acid baths required by the samples processing. The basic condition for the mask material is to be resistant to HF that we employ as etchant of the  $\text{SrTiO}_3$  substrate. Several complex oxides are suitable for this task, but here we choose  $(\text{La,Sr})\text{MnO}_3$  (LSMO), a magnetic compound proposed for several device applications [29, 37–39]. LSMO hard masks are deposited on both sides by pulsed laser deposition as discussed in our previous works [40]. A critical point of this method is the han-

\* nicola.manca@spin.cnr.it

dling of the substrate that enables deposition of the material on both its sides. Since the STO is clamped to a stainless steel holder that would contaminate the back-side during the growth, we place a second STO substrate in-between the sample and the holder. This second layer introduces a slightly increased thermal resistance from the sample holder to the growth substrate, which has to be taken into account setting up the deposition conditions. Patterning of both layers is realized by standard UV lithography as discussed in the “Experimental Section”. The top and bottom patterns were aligned to each other using the optical microscope integrated in the mask aligner, taking advantage of the transparency of the STO substrate.

### A. Etching rates calibration

The realization of a desired device geometries is only possible by careful designing the hard mask and device layers and this, in turn, requires the knowledge of the etching evolution along different lattice directions. Previous studies indicate that the out-of-plane etching rate of STO in 5 % HF water solution at 30 °C is 13.5  $\mu\text{m}/\text{h}$  for (001) substrates and 9  $\mu\text{m}/\text{h}$  for (110) substrates.[40] This means that etching through a 100  $\mu\text{m}$ -thick substrate requires more than 7 h for STO(001) and more than 11 h for STO(110). Moreover, STO dissolution in HF results in by-products which are not soluble and during long etching process the STO surfaces becomes progressively clogged, with a lowering of the dissolution rate and the accumulation of residues which are difficult to remove afterwards. To overcome these issues we employed an acid solution consisting of a mixture of 5 % HF and 5 %  $\text{H}_3\text{PO}_4$  in purified water which is kept at 40 °C. The higher temperature speeds up the etching rate, while we observed that  $\text{H}_3\text{PO}_4$  improves the cleanliness of the final structures by reducing the amount of the deposited etching by-products.

To calibrate the etching rates in these experimental conditions, we prepared two samples by depositing a 100 nm-thick LSMO layer on both sides of a STO(001) and a STO(110) substrate. For each sample, we realized an aperture in the top layer, exposing the STO substrates, and then periodically monitored the size of the resulting pit while soaking the samples in the acid bath. The geometries of the apertures are shown in the schematic illustrations of Fig. 1a and b, and were chosen based on a previous study reported in Ref. [40]. For the STO(001) case, it is a  $500 \times 500 \mu\text{m}^2$  square window rotated by 45° with respect to the sample’s edges, i.e. the  $\langle 110 \rangle$  directions. This is because, for this cut-plane, having the edges aligned to  $\langle 110 \rangle$  lattice directions preserve their orientation during the etching process, resulting in good reproducibility. For the STO(110) case, instead, the in-plane etching is anisotropic and we thus employed a  $250 \times 500 \mu\text{m}^2$  rectangular window whose short/long edges are aligned to the fast/slow etching

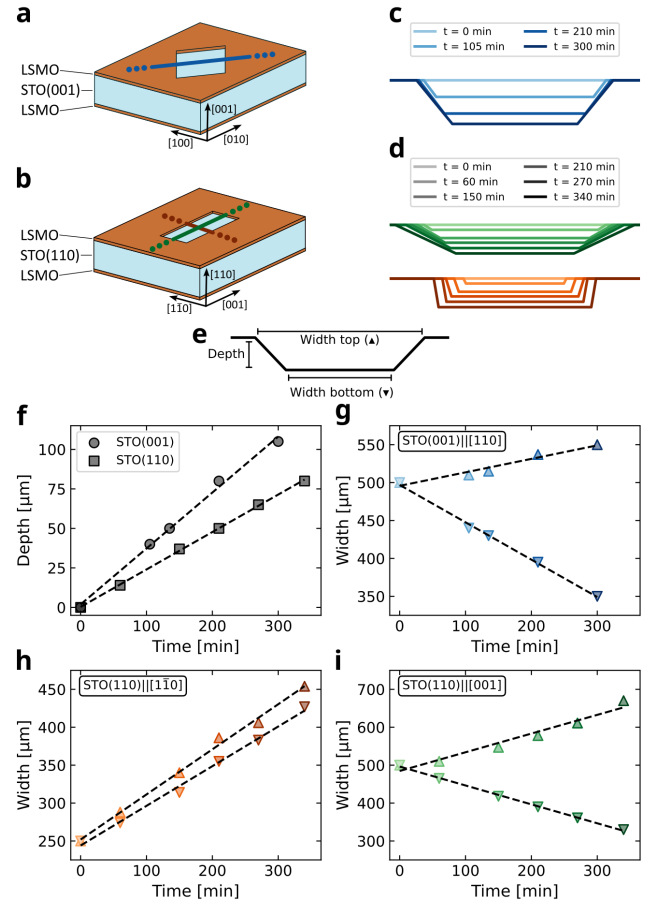


FIG. 1. Calibration of the etching rates of  $\text{SrTiO}_3(001)$  and (110) substrates. (a, b) Schematic of the two samples used to calibrate the rates. STO is light blue, LSMO is brown, and the cut-lines indicate the directions along which the (c) and (d) profiles were measured. (c, d) Time evolution of the pit profiles along the cross-sections in (a) and (b). (e) Diagram of the geometric parameters monitored during the etching process. (f)–(i) Time evolution of the depth (○, □), the top width (Δ), and the bottom width (▽) of the pits geometry as shown in (e). Cut-plane and cross-section direction are indicated by labels in each panel. The colors of the data-point in (g)–(i) correspond to those in (c) and (d).

directions. The size of the apertures was large enough to be sure that they would maintain their shape along the whole etching time (about 7 hours) while still being fully visible within the field of view of the microscope for measuring their size.

The geometric parameters of the pit formed in the LSMO apertures during the wet etching process are measured along the cut-lines indicated in Fig. 1a and b, which are aligned with the following directions: STO(001)||[110] (blue), STO(110)||[001] (green), and STO(110)||[110] (red). These colors are used consistently across Fig. 1. All the reconstructed profiles are reported Fig. 1c and d. They show the time evolution of the etching front along the different lattice directions and provide a direct comparison between the side-walls slope of the aperture and the widening of the hard mask

Cut-plane	Direction	Position	$r_{p/\perp}$ [ $\mu\text{m}/\text{min}$ ]
(001)	[001]	depth	$+0.35 \pm 0.04$
	$\langle 110 \rangle$	top	$+0.18 \pm 0.02$
	$\langle 110 \rangle$	bottom	$-0.49 \pm 0.05$
(110)	[110]	depth	$+0.24 \pm 0.02$
	$\langle 001 \rangle$	top	$+0.49 \pm 0.05$
	$\langle 001 \rangle$	bottom	$-0.50 \pm 0.05$
	$\langle 1\bar{1}0 \rangle$	top	$+0.59 \pm 0.06$
	$\langle 1\bar{1}0 \rangle$	bottom	$+0.52 \pm 0.05$

TABLE I. Etching rates of  $\text{SrTiO}_3$  in HF 5% +  $\text{H}_3\text{PO}_4$  5% in  $\text{H}_2\text{O}$  at 40 °C. Different etching “directions” and “positions” are referred to the illustrations of Fig. 1a, b, and e. Numerical values corresponds to the slopes of the linear fits (black dashed lines) reported in Fig. 1f–h.

window determined by etching anisotropy. It is noteworthy that the  $\text{STO}(110)$  sidewalls get progressively aligned to specific directions. Along the  $[1\bar{1}0]$  profile (red) they are almost vertical, while along the  $[001]$  profile (green) we observe a slow evolution towards a slope of 25°. For the  $\text{STO}(001)$  case, instead, the four sidewalls of the aperture are all equivalent because of symmetry and all the sidewalls have a slope of about  $\sim 45^\circ$ . We point out that these angles are the average slope of the sidewalls and, for such large scales, are not directly related to specific crystallographic planes.

The shape of an aperture in  $\text{STO}$  at the end of the etching process, i.e. when the full thickness of the substrate is dissolved, can be predicted by knowing the time evolution of the depth, the top width, and the bottom width of the aperture, as schematically illustrated in Fig. 1e. In this context, the main parameter is the out-of-plane etching rate ( $r_\perp$ ), determining the time ( $\Delta t$ ) required to cover the thickness of a substrate ( $d$ ). The top/bottom width of the aperture after  $\Delta t$  can be calculated as

$$w_f = w_i + r_p \Delta t; \Delta t = d/r_\perp \quad (1)$$

where  $r_p$  is the in-plane etching rate, and  $w_{i/f}$  the initial/final width value. The time evolution of the aperture depth for both the substrates is reported in Fig. 1f, while the time dependence of the top ( $\Delta$ ) and bottom ( $\nabla$ ) width of the apertures is reported in Fig. 1g–i, where each panel shows one of the lattice directions corresponding to the cut-lines of Fig. 1a, b. Etching rates are obtained from a linear fit of these data and are reported in Table I, where positive/negative values along the in-plane directions correspond to widening/narrowing of the initial window width. We point out that these rates critically depend on parameters that are difficult to control at present, such as the fluid speed at the  $\text{STO}$  surface or the density of crystal defects. This gives rise to an estimated uncertainty in the etch rate of 10%

## B. Fabrication protocol of through-hole devices

Figure 2a shows a schematic step-by-step illustration of the fabrication protocol employed to realize oxide devices suspended on through-hole  $\text{STO}$  substrates.

The first step of the process is to thin down the substrate below the patterned device. This is required because a full etching of the substrate starting from top would result in an excessive under-etching. Back-side etching is performed in a custom Polytetrafluoroethylene (PTFE) sample holder as is depicted in Fig. 2b. It has a hole at its center with diameter of  $\sim 3\text{ mm}$  to let the acid solution reaching the sample. This hole is smaller than the typical substrate size (5 mm) to prevent spillover to the edges. The holder is placed in a PTFE cup containing the acid solution, which is kept at 40 °C in bain-marie and agitated by a magnetic stirrer at about 200 RPM. Since during this process both sides of the sample are already patterned, the unprotected  $\text{STO}$  on the top surface could be affected by HF vapors. To prevent this issue, we deposit a protection layer of SPR-220-4.5 photo-resist on the top surface of the sample. Other compounds can be also employed, as long as they have good adhesion, are resistant to HF, and allow for easy removal. When the thickness of the substrate in the hard mask aperture is below 20  $\mu\text{m}$ , the sample is washed in distilled water. The protection layer is then removed from the top surface by ultrasonic bath in acetone and then ethanol. The final etching step consists in soaking the sample in the acid solution (5% HF + 5%  $\text{H}_3\text{PO}_4$  in distilled water). To do so we employ a transparent polypropylene holder (see Fig. 2c) with same temperature and agitation conditions as in the back-side etching step. This final step was implemented to suspend the device on the top layer before the opening of the hole across the substrate, which could otherwise affect the

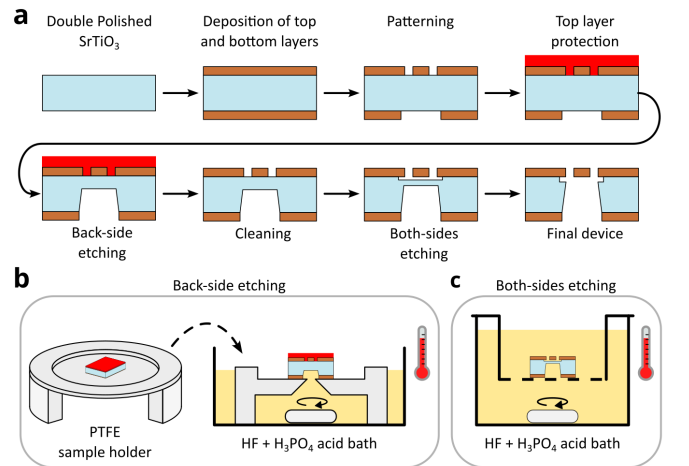


FIG. 2. Fabrication protocol of through-hole suspended devices on single crystal  $\text{SrTiO}_3$  substrates. (a) Main steps of the substrate micro-machining process. Schematic illustrations of (b) the setup for back-side wet etching and (c) the final wet etching step by full soaking the sample.



fabrication yield. Once the through-hole is complete, the sample is dried in a CO<sub>2</sub> critical point drying system.

### C. Trampoline resonators with backside aperture

The fabrication protocol reported in Fig. 2 is employed to realize suspended trampoline resonators of LSMO. We take advantage from the etching anisotropy of STO(110) to control the width of the aperture in the substrate just below the suspended structure. To do so, we employed two identical samples having 100 nm-thick LSMO films deposited on the top and bottom surfaces. The top layers are patterned as an array of trampolines having central square pad of  $20 \times 20 \mu\text{m}^2$  and 100  $\mu\text{m}$ -long tethers. The bottom layers are patterned as a 200  $\mu\text{m}$ -wide slot, but in one case the slot width is aligned along the  $[1\bar{1}0]$  direction while in the other along the  $[100]$  direction. Figure 3a and b show an optical micrograph of the patterned LSMO layers (in transmitted light) and one of the final devices, together with schematic illustrations of the corresponding transversal section. In Fig. 3a the trench got wider during the etching process, in agreement with the positive etching rate in Table I, and the trampoline gets fully exposed from the bottom side. In Fig. 3b, instead, the final aperture is just a narrow trench in the substrate, whose width was calibrated to correspond to the size of the trampoline's pad. To do so, accordingly with Eq. (1), we first removed 70  $\mu\text{m}$  of substrate by back-side etching (Fig. 2b, leaving a trench width of about 55  $\mu\text{m}$ ). We then removed the last 40  $\mu\text{m}$  by both-sides etching (Fig. 2c), this further narrows the trench for only half of the etched thickness, making it about 20  $\mu\text{m}$ -wide. We note that this kind of device geometry allows to employ the residual substrate as an hard mask for the deposition of additional layers on just the backside of the trampoline. This could be helpful to preserve the mechanical properties of the resonator, minimizing the added mass to the pad region and without affecting the stress state of the tethers. Despite the narrow aperture, it is possible to probe the motion of the LSMO trampoline from the backside. To do so, we employ the setup schematically reported in Fig. 3c and described in the "Experimental Section". The response when the device is driven around the first mechanical resonance is shown in Fig. 3d, together with the fit of magnitude (blue) and phase (orange) to a damped driven harmonic oscillator (black dashed line). The  $Q$ -factor is about 11700, which is in the ballpark of previous reports on similar devices, indicating that the fabrication process did not critically affect the mechanical properties [27].

### D. Sealed oxide membrane

A simple modification of the bulk micromachining protocol described above allows for the realization of

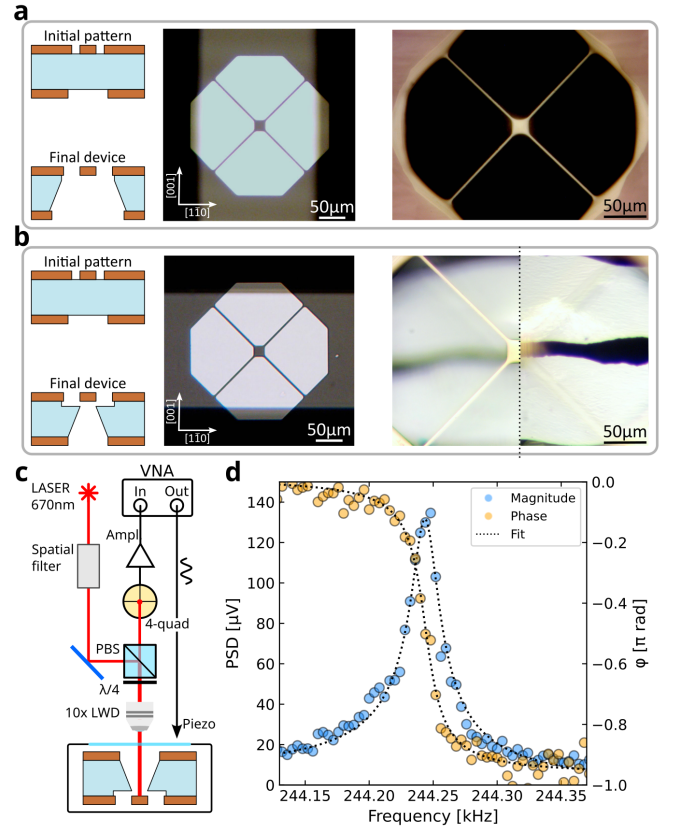


FIG. 3. Free-hanging trampoline with controlled aperture width in SrTiO<sub>3</sub>(110). (a, b) Schematic of the process, hard mask alignment and final device with short edge parallel to the (a)  $[1\bar{1}0]$  or (b)  $[001]$  direction. The device in (b) is shown for the focal planes of the trampoline (left) and the trench (right), located about 20  $\mu\text{m}$  below. (c) Schematic of the optical setup used to measure the motion of the trampoline in (b). Details are reported in the "Experimental Section". (d) Spectrum of the first resonance mode (circles). Lorentzian fit (dashed line) indicates a  $Q$ -factor of 11700.

another kind of devices: clamped membranes. In this case the protocol reported in Fig. 4 is slightly modified and only the bottom layer undergoes a lithographic process. The schematic illustration of the initial and the final geometry of the sample is shown in Fig. 4a. It was made of 100 nm-thick LSMO films deposited on both sides of a 105  $\mu\text{m}$ -thick STO(001) substrate. The bottom layer was patterned as a square hole rotated by 45°, similarly to Fig. 1a, with a side length of 200  $\mu\text{m}$ . The sample was etched from one side, as shown in Fig. 2b, with the top layer protected by SPR-220-4.5 photoresist, which was removed in acetone at the end of the process. The total etching time was 270 min, resulting in a square membrane with 80  $\mu\text{m}$ -long edges parallel to those of the initial hard mask. Fig. 4b and c are optical micrograph of the membrane at the end of the fabrication process seen in reflected light from top and bottom, respectively. The edges of the membrane are not perfectly straight. This is probably due to a slight misalignment of the initial pattern with respect to the nominal 45° ori-

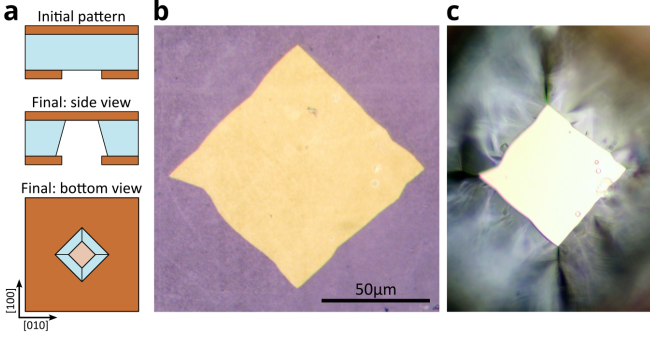


FIG. 4. LSMO clamped membrane. (a) Schematic illustration of the initial and final sample geometry. (b, c) Optical micrograph of the LSMO membrane seen from (b) top and (c) bottom in reflected light (not to-scale).

entation. Here, crystal defects also play a role, acting as seeding points for etch pits and locally enhancing the corrosion rate during the process. We note that the etching rates observed during the fabrication of this device are slightly different to those reported in Table I. This is expected because, beyond the previously discussed uncertainty in the measured etching rates, in this case the etching is just from one side, as described in Fig. 2b, while values reported in Table I were calibrated in soaking condition, as in Fig. 2c. Improved reproducibility can be obtained by calibrating the etching time for specific hard mask geometry and etching process.

### E. Bulk $\text{SrTiO}_3$ trampoline

If, contrarily to the previous cases, the oxides thin films deposited on both the surfaces are employed as hard masks, suspended devices entirely made from STO substrate can be fabricated. This is demonstrated in Figure 5, showing a trampoline carved from a 110 μm-thick  $\text{STO}(110)$  substrate. The main steps of the fabrication protocol are reported in Fig. 5a, where, contrary to the previous cases, the oxides thin films deposited on both the surfaces are employed as hard masks. The top layer is patterned as trampoline, similarly to what reported in Fig. 3, but in this case the geometry is enlarged: the tethers are 350 μm-long and have a width of 35 μm, while the central pad is  $100 \times 100 \mu\text{m}^2$ . The bottom mask is a  $500 \times 750 \mu\text{m}^2$  rectangular aperture. Such widening is required to let the STO structure be resilient to the under-etching during the second etching phase, when the sample is soaking in the acid bath (Fig. 2c). Since the corrosion happens both in-plane and out-of-plane, and the corresponding rates are comparable, the width of the hard mask shall be comparable to the thickness of the substrate still to be etched, i.e. few tens of micrometers. This guarantees a continuous flat surface even in the presence of defects that may locally enhance in-plane the etching rate [40]. The last fabrication step is peculiar to this process and consists in soaking the sample in 4.5 % HCl in water solution. This dissolves the LSMO

masks, exposing the surface of the STO substrate [16].

Fig. 5b shows the final device as seen from the top. The thickness of the suspended structure is about 5 μm. The black oval region is the aperture across the STO substrate, with at its center the pad of the bulk STO trampoline. The residual frame shows areas having different colors, from white to gray. This is due to the microscope light reflecting from facets in the backside mask, where small defects triggered unintended etching processes. The width of this aperture is smaller than the length of the tethers. This mismatch can be tuned by controlling the duration of the first etching step, where a longer corrosion produces longer tethers. However, since the tethers get narrower over time, longer etching times may hinder the structural integrity or the surface quality. Because of this, the realization of desired device geometries requires precise design and alignment of both top and bottom hard masks. Fig. 5c is a magnification of the central region of the trampoline, where it is possible to observe the effect of etching anisotropy to the sides of the formerly square pad. While the vertical edges are still straight, the horizontal ones got rounded towards the tethers' clamping points. On the pad it is also visible crystal faceting, this happens on the bottom surface, about 5 μm below, and is due to the long etching

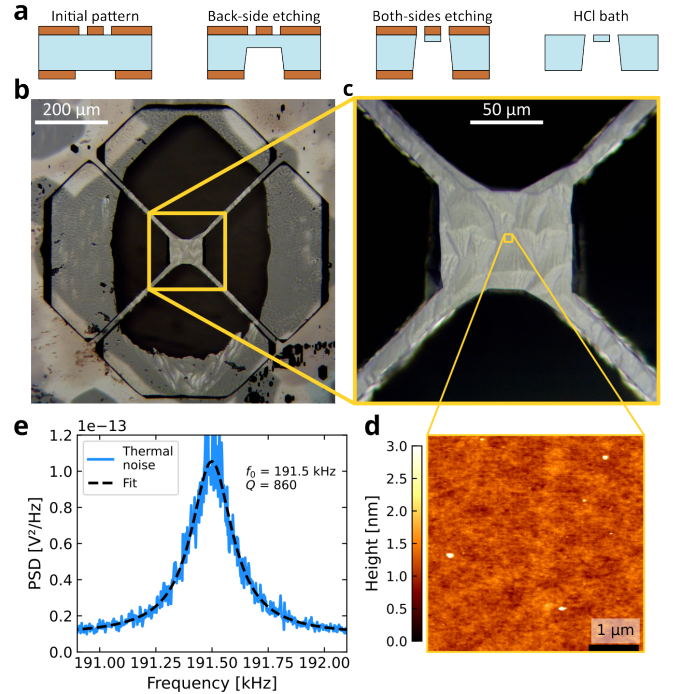


FIG. 5. Bulk micro-machining of a  $\text{SrTiO}_3(110)$  substrate. (a) Main steps of the fabrication process. (b) Suspended trampoline made from  $\text{SrTiO}_3(110)$  substrate, where the black oval region is the open aperture. (c) Magnification of the pad region. The residual thickness is about 5 μm, making the faceting of the bottom surface visible. (d) Surface topography measured by atomic force microscope showing a RMS roughness below 0.3 nm. (e) Thermal noise spectrum showing the first mechanical mode.

process. The quality of the top surface of the bulk STO trampoline was inspected by atomic force microscopy. The surface morphology of a  $5 \times 5 \mu\text{m}^2$  region at the center of the suspended pad is reported in Fig. 5d. It shows a smooth surface with RMS roughness below 0.3 nm and low density of residual cluster defects. Here, presence of sharp terraces is not expected because the substrate was not terminated and had no thermal treatments.

This suspended trampoline can be employed to realize new types of oxide-based MEMS. It is thus relevant to characterize its basic mechanical properties. Fig. 5e shows the noise power spectral density around the frequency corresponding to the first mechanical mode of the STO trampoline measured using a fiber interferometer. The measured data are reported as a blue line, while the black dashed line is the best fit of the function describing the thermal noise power spectrum of a mechanical resonator [41]. The extracted quality factor ( $Q$ -factor) is of about 850, which is rather small if compared to other complex oxide systems [23, 27, 42]. One reason for this is the absence of tensile strain [43], as the trampoline is made of the very material of its supporting frame. Another possible reason is the geometry of the tethers which have slightly different lengths and bulky clamping points with a wedge shape, where the trampoline smoothly fade into the substrate. Because of that, this resonator is not well-isolated from its frame, likely increasing the mechanical energy losses. These aspects could be partially improved by careful design of the clamping points and backside aperture geometries.

The fabrication of bulk STO trampolines allows to obtain engineered growth templates compatible surface-reconstruction processes, such as annealing or termination in buffered-HF. This offers the possibility to grow oxide thin films on top of  $\text{SrTiO}_3$  substrates having the same crystal quality as commercial ones, but with much higher aspect ratio, making possible to design new experiments based, as an example, on the interplay between oxide interfacial systems and mechanical characterizations, thermal transport, or strain measurements.

### III. CONCLUSIONS

In conclusion, we presented a fabrication protocol to realize a new class of suspended devices from complex oxides thin films deposited on top of  $\text{SrTiO}_3$  substrates. We provided the wet etching rate of the  $\text{SrTiO}_3$ (001) and (110) substrates in controlled conditions, which are instrumental to the design of hard masks geometry and predict the resulting aperture characteristics. To show the potential of this approach in realizing different kind of full-oxide devices, we discussed three examples of device geometry all realized using LSMO as hard mask and device layer. The detailed description of the fabrication steps allows for a facile extensions of this protocol to different device geometries and compounds.

## IV. EXPERIMENTAL SECTION

*UV lithography:* Patterning of the LSMO hard masks is performed by UV lithography followed by Ar ions dry etching. SPR-220-4.5 photo-resist is spin-coated at 6000 RPM for 45 s and then baked at  $120^\circ\text{C}$  for 150 s. Dry etching time is about 45 min, with an ion energy of 500 eV and a current density of  $0.2 \text{ mA}/\text{cm}^2$ . Then, photo-resist residues are removed by ultrasonic baths in acetone and then ethanol at room temperature.

*Etching rates measurements:* The geometric parameters of the pits that were measured are depth, top width and bottom width at different times. In-plane measurements were obtained from optical micrographs taking the initial LSMO mask as reference for scale calibration. Depth was measured by focal distance between the top and bottom plane at each time, with an absolute error of  $\sim 1 \mu\text{m}$ . Reported profiles are obtained as line plots connecting these measured points in a  $xy$  plane.

*Mechanical Measurements:* Backside mechanical measurements of the LSMO trampoline resonators were acquired in a custom setup based on the optical lever detection scheme. It includes a 670 nm laser, a polarizing beam splitter (PBS), a quarter-wave plate ( $\lambda/4$ ), a  $\times 10$  Long Working Distance objective lens (LWD), and a custom-made four-quadrant photo-diode. Background pressure was  $2 \cdot 10^{-5}$  mbar and temperature kept at the constant value of  $25^\circ\text{C}$ . Vector network analyzer (VNA) is a HP Agilent 4395A. Mechanical measurements of the bulk  $\text{SrTiO}_3$ (110) trampoline were conducted using a fiber interferometer operating at 1550 nm at a pressure below  $10^{-4}$  mbar and at room temperature.

## ACKNOWLEDGEMENTS

We thank Alberto Martinelli for useful discussion on the chemistry of the etching process. This work was carried out under the OXiNEMS project ([www.oxinems.eu](http://www.oxinems.eu)). This project has received funding from the European Union's Horizon 2020 research and innovation programme under Grant Agreement No. 828784. This work was carried out within the framework of the project "RAISE - Robotics and AI for Socio-economic Empowerment" and has been supported by European Union - NextGenerationEU. We acknowledge financial support by MUR under the National Recovery and Resilience Plan (NRRP), Project "Network 4 Energy Sustainable Transition - NEST" (PE0000021).

## OPEN DATA

The numerical data shown in figures of the manuscript and the supplemental material can be downloaded from the Zenodo online repository: <https://dx.doi.org/10.5281/zenodo.13898651>



- [1] S. R. Bakaul, C. R. Serrao, M. Lee, C. W. Yeung, A. Sarker, S.-L. Hsu, A. K. Yadav, L. Dedon, L. You, A. I. Khan, J. D. Clarkson, C. Hu, R. Ramesh, and S. Salahuddin, Single crystal functional oxides on silicon, *Nat Commun* **7**, 10547 (2016).
- [2] D. M. Paskiewicz, R. Sichel-Tissot, E. Karapetrova, L. Stan, and D. D. Fong, Single-Crystalline SrRuO<sub>3</sub> Nanomembranes: A Platform for Flexible Oxide Electronics, *Nano Lett.* **16**, 534 (2016).
- [3] L. Shen, L. Wu, Q. Sheng, C. Ma, Y. Zhang, L. Lu, J. Ma, J. Ma, J. Bian, Y. Yang, A. Chen, X. Lu, M. Liu, H. Wang, and C.-L. Jia, Epitaxial Lift-Off of Centimeter-Scaled Spinel Ferrite Oxide Thin Films for Flexible Electronics, *Adv. Mater.* **29**, 1702411 (2017).
- [4] Y. Higuchi, T. Kanki, and H. Tanaka, Formation of single-crystal VO<sub>2</sub> thin films on MgO(110) substrates using ultrathin TiO<sub>2</sub> buffer layers, *Appl. Phys. Express* **11**, 085503 (2018).
- [5] X. Li, Z. Yin, X. Zhang, Y. Wang, D. Wang, M. Gao, J. Meng, J. Wu, and J. You, Epitaxial Lifting of Wafer-Scale VO<sub>2</sub> Nanomembranes for Flexible, Ultrasensitive Tactile Sensors, *Adv. Mater. Technol.* **4**, 1800695 (2019).
- [6] D. Lu, D. J. Baek, S. S. Hong, L. F. Kourkoutis, Y. Hikita, and H. Y. Hwang, Synthesis of freestanding single-crystal perovskite films and heterostructures by etching of sacrificial water-soluble layers, *Nature Mater* **15**, 1255 (2016).
- [7] A. Sambri, M. Scuderi, A. Guarino, E. D. Gennaro, R. Erlandsen, R. T. Dahm, A. V. Bjørli, D. V. Christensen, R. D. Capua, B. D. Ventura, U. S. D. Uccio, S. Mirabella, G. Nicotra, C. Spinella, T. S. Jespersen, and F. M. Granozio, Self-Formed, Conducting LaAlO<sub>3</sub>/SrTiO<sub>3</sub> Micro-Membranes, *Adv. Funct. Mater.* **30**, 1909964 (2020).
- [8] R. Erlandsen, R. T. Dahm, F. Trier, M. Scuderi, E. Di Gennaro, A. Sambri, C. K. Reffeldt Kirchert, N. Pryds, F. M. Granozio, and T. S. Jespersen, A Two-Dimensional Superconducting Electron Gas in Freestanding LaAlO<sub>3</sub>/SrTiO<sub>3</sub> Micromembranes, *Nano Lett.* **22**, 4758 (2022).
- [9] G. Niu, G. Saint-Girons, B. Vilquin, G. Delhay, J.-L. Maurice, C. Botella, Y. Robach, and G. Hollinger, Molecular beam epitaxy of SrTiO<sub>3</sub> on Si (001): Early stages of the growth and strain relaxation, *Appl. Phys. Lett.* **95**, 062902 (2009).
- [10] J. W. Reiner, A. M. Kolpak, Y. Segal, K. F. Garrity, S. Ismail-Beigi, C. H. Ahn, and F. J. Walker, Crystalline Oxides on Silicon, *Adv. Mater.* **22**, 2919 (2010).
- [11] S.-H. Baek and C.-B. Eom, Epitaxial integration of perovskite-based multifunctional oxides on silicon, *Acta Materialia* **61**, 2734 (2013).
- [12] K. Liu, C. Cheng, J. Suh, R. Tang-Kong, D. Fu, S. Lee, J. Zhou, L. O. Chua, and J. Wu, Powerful, Multifunctional Torsional Micromuscles Activated by Phase Transition, *Adv. Mater.* **26**, 1746 (2014).
- [13] D. Torres, T. Wang, J. Zhang, X. Zhang, S. Dooley, X. Tan, H. Xie, and N. Sepulveda, VO<sub>2</sub>-Based MEMS Mirrors, *J. Microelectromech. Syst.* **25**, 780 (2016).
- [14] K. Dong, H. S. Choe, X. Wang, H. Liu, B. Saha, C. Ko, Y. Deng, K. B. Tom, S. Lou, L. Wang, C. P. Grigoropoulos, Z. You, J. Yao, and J. Wu, A 0.2 V Micro-Electromechanical Switch Enabled by a Phase Transition, *Small* **14**, 1703621 (2018).
- [15] M. Spreitzer, D. Klement, T. Parkelj Potočnik, U. Trstenjak, Z. Jovanović, M. D. Nguyen, H. Yuan, J. E. ten Elshof, E. Houwman, G. Koster, G. Rijnders, J. Fompeyrine, L. Kornblum, D. P. Fenning, Y. Liang, W.-Y. Tong, and P. Ghosez, Epitaxial ferroelectric oxides on silicon with perspectives for future device applications, *APL Materials* **9**, 040701 (2021).
- [16] L. Pellegrino, M. Biasotti, E. Bellingeri, C. Bernini, A. S. Siri, and D. Marré, All-Oxide Crystalline Microelectromechanical Systems: Bending the Functionalities of Transition-Metal Oxide Thin Films, *Adv. Mater.* **21**, 2377 (2009).
- [17] C. Deneke, E. Wild, K. Boldyreva, S. Baunack, P. Cendula, I. Mönch, M. Simon, A. Malachias, K. Dörr, and O. G. Schmidt, Rolled-up tubes and cantilevers by releasing SrRuO<sub>3</sub>-Pr<sub>0.7</sub>Ca<sub>0.3</sub>MnO<sub>3</sub> nanomembranes, *Nanoscale Res Lett* **6**, 621 (2011).
- [18] N. Manca, L. Pellegrino, and D. Marré, Reversible oxygen vacancies doping in (La<sub>0.7</sub>Sr<sub>0.3</sub>)MnO<sub>3</sub> microbridges by combined self-heating and electromigration, *Appl. Phys. Lett.* **106**, 203502 (2015).
- [19] N. Manca, T. Kanki, H. Tanaka, D. Marré, and L. Pellegrino, Influence of thermal boundary conditions on the current-driven resistive transition in VO<sub>2</sub> microbridges, *Appl. Phys. Lett.* **107**, 143509 (2015).
- [20] S. S. Hong, M. Gu, M. Verma, V. Harbola, B. Y. Wang, D. Lu, A. Vailionis, Y. Hikita, R. Pentcheva, J. M. Rondinelli, and H. Y. Hwang, Extreme tensile strain states in La<sub>0.7</sub>Ca<sub>0.3</sub>MnO<sub>3</sub> membranes, *Science* **368**, 71 (2020).
- [21] R. Xu, J. Huang, E. S. Barnard, S. S. Hong, P. Singh, E. K. Wong, T. Jansen, V. Harbola, J. Xiao, B. Y. Wang, S. Crossley, D. Lu, S. Liu, and H. Y. Hwang, Strain-induced room-temperature ferroelectricity in SrTiO<sub>3</sub> membranes, *Nat Commun* **11**, 3141 (2020).
- [22] D. Davidovikj, D. J. Groenendijk, A. M. R. V. L. Monteiro, A. Dijkhoff, D. Afanasiev, M. Šiškins, M. Lee, Y. Huang, E. van Heumen, H. S. J. van der Zant, A. D. Caviglia, and P. G. Steeneken, Ultrathin complex oxide nanomechanical resonators, *Commun Phys* **3**, 163 (2020).
- [23] N. Manca, G. Tarsi, A. Kalaboukhov, F. Bisio, F. Cagliaris, F. Lombardi, D. Marré, and L. Pellegrino, Strain, Young's modulus, and structural transition of EuTiO<sub>3</sub> thin films probed by micro-mechanical methods, *APL Mater.* **11**, 101107 (2023).
- [24] N. Manca, G. Mattoni, M. Pelassa, W. J. Venstra, H. S. J. van der Zant, and A. D. Caviglia, Large Tunability of Strain in WO<sub>3</sub> Single-Crystal Microresonators Controlled by Exposure to H<sub>2</sub> Gas, *ACS Appl. Mater. Interfaces* **11**, 44438 (2019).
- [25] M. Lee, M. P. Robin, R. H. Guis, U. Filippozzi, D. H. Shin, T. C. van Thiel, S. P. Paardekoooper, J. R. Renshof, H. S. J. van der Zant, A. D. Caviglia, G. J. Verbiest, and P. G. Steeneken, Self-Sealing Complex Oxide Resonators, *Nano Lett.* **22**, 1475 (2022).
- [26] N. Manca, L. Pellegrino, T. Kanki, W. J. Venstra, G. Mattoni, Y. Higuchi, H. Tanaka, A. D. Caviglia, and D. Marré, Selective High-Frequency Mechanical Actuation Driven by the VO<sub>2</sub> Electronic Instability, *Adv. Mater.* **29**, 1701618 (2017).
- [27] N. Manca, F. Remaggi, A. E. Plaza, L. Varbaro, C. Bernini, L. Pellegrino, and D. Marré, Stress Analysis and Q-Factor

- of Free-Standing (La,Sr)MnO<sub>3</sub> Oxide Resonators, *Small* **18**, 2202768 (2022).
- [28] L. Méchin, J.-C. Villégier, and D. Bloyet, Suspended epitaxial YBaCuO microbolometers fabricated by silicon micromachining: Modeling and measurements, *Journal of Applied Physics* **81**, 7039 (1997).
- [29] V. M. Nascimento, L. Méchin, S. Liu, A. Aryan, C. Adamo, D. G. Schlom, and B. Guillet, Electro-thermal and optical characterization of an uncooled suspended bolometer based on an epitaxial La<sub>0.7</sub>Sr<sub>0.3</sub>MnO<sub>3</sub> film grown on CaTiO<sub>3</sub>/Si, *J. Phys. D: Appl. Phys.* **54**, 055301 (2021).
- [30] N. Manca, T. Kanki, F. Endo, D. Marré, and L. Pellegrino, Planar Nanoactuators Based on VO<sub>2</sub> Phase Transition, *Nano Lett.* **20**, 7251 (2020).
- [31] N. Manca, T. Kanki, F. Endo, E. Ragucci, L. Pellegrino, and D. Marré, Anisotropic Temperature-Driven Strain Dynamics in VO<sub>2</sub> Solid-State Microactuators, *ACS Appl. Electron. Mater.* **3**, 211 (2021).
- [32] R. Takahashi and M. Lippmaa, Sacrificial Water-Soluble BaO Layer for Fabricating Free-Standing Piezoelectric Membranes, *ACS Appl. Mater. Interfaces* **12**, 25042 (2020).
- [33] M. Lee, J. R. Renshof, K. J. van Zeggeren, M. J. A. Houmes, E. Lesne, M. Šiškins, T. C. van Thiel, R. H. Guis, M. R. van Blankenstein, G. J. Verbiest, A. D. Caviglia, H. S. J. van der Zant, and P. G. Steeneken, Ultrathin Piezoelectric Resonators Based on Graphene and Free-Standing Single-Crystal BaTiO<sub>3</sub>, *Advanced Materials* **34**, 2204630 (2022).
- [34] S. Ganguly, D. Pesquera, D. M. Garcia, U. Saeed, N. Mirzamohammadi, J. Santiso, J. Padilla, J. M. C. Roque, C. Laulhé, F. Berenguer, L. G. Villanueva, and G. Catalan, Photostrictive Actuators Based on Freestanding Ferroelectric Membranes, *Adv. Mater.* **36**, 2310198 (2024).
- [35] A. Corigliano, *Mechanics of Microsystems*, Microsystem and Nanotechnology Series No. 7646 (Wiley, Hoboken, 2018).
- [36] E. Romero, V. M. Valenzuela, A. R. Kermany, L. Sementilli, F. Iacopi, and W. P. Bowen, Engineering the Dissipation of Crystalline Micromechanical Resonators, *Phys. Rev. Applied* **13**, 044007 (2020).
- [37] C. Zhang, S. Ding, K. Qiao, J. Li, Z. Li, Z. Yin, J. Sun, J. Wang, T. Zhao, F. Hu, and B. Shen, Large Low-Field Magnetoresistance (LFMR) Effect in Free-Standing La<sub>0.7</sub>Sr<sub>0.3</sub>MnO<sub>3</sub> Films, *ACS Appl. Mater. Interfaces* **13**, 28442 (2021).
- [38] A. Vera, I. Martínez, L. G. Enger, B. Guillet, R. Guerrero, J. M. Díez, O. Rousseau, M. Lam Chok Sing, V. Pierron, P. Perna, J. J. Hernández, I. Rodríguez, I. Calaresu, A. Meier, C. Huck, A. Domínguez-Bajo, A. González-Mayorga, E. López-Dolado, M. C. Serrano, L. Ballerini, L. Pérez, R. Miranda, S. Flament, M. T. González, L. Méchin, and J. Camarero, High-Performance Implantable Sensors based on Anisotropic Magnetoresistive La<sub>0.67</sub>Sr<sub>0.33</sub>MnO<sub>3</sub> for Biomedical Applications, *ACS Biomater. Sci. Eng.* **9**, 1020 (2023).
- [39] L. G. Enger, S. Flament, I. N. Bhatti, O. Rousseau, B. Guillet, M. L. C. Sing, V. Pierron, S. Lebargy, S. K. Chaluvadi, B. Domengés, A. Vera, J. M. Díez, I. Martínez, R. Guerrero, L. Pérez, M. T. Gonzalez, R. Miranda, J. Camarero, P. Perna, and L. Méchin, Key Parameters for Detectivity Improvement of Low Noise Anisotropic Magnetoresistive Sensors Made of La<sub>2</sub>/3Sr<sub>1</sub>/3MnO<sub>3</sub> Single Layers on Vicinal Substrates, *ACS Appl. Electron. Mater.* **5**, 729 (2023).
- [40] A. E. Plaza, N. Manca, C. Bernini, D. Marré, and L. Pellegrino, The role of etching anisotropy in the fabrication of freestanding oxide microstructures on SrTiO<sub>3</sub>(100), SrTiO<sub>3</sub>(110), and SrTiO<sub>3</sub>(111) substrates, *Appl. Phys. Lett.* **119**, 033504 (2021).
- [41] B. Hauer, C. Doolin, K. Beach, and J. Davis, A general procedure for thermomechanical calibration of nano/micromechanical resonators, *Annals of Physics* **339**, 181 (2013).
- [42] N. Manca, A. Kalaboukhov, A. E. Plaza, L. Cichetto Jr., E. Wahlberg, E. Bellingeri, F. Bisio, F. Lombardi, D. Marré, and L. Pellegrino, Integration of High-Tc Superconductors with High-Q-Factor Oxide Mechanical Resonators, *Adv. Func. Mater.* **n/a**, 2403155 (2024).
- [43] L. Sementilli, E. Romero, and W. P. Bowen, Nanomechanical Dissipation and Strain Engineering, *Adv. Funct. Materials* **32**, 2105247 (2022).